SHOCK SOLUTIONS FOR HIGH CONCENTRATION PARTICLE-LADEN THIN FILMS*

LI WANG † AND ANDREA L. BERTOZZI ‡

Abstract. We study the shock dynamics for a recently proposed system of conservation laws (Murisic et. al [J. Fluid Mech. 2013]) describing gravity-driven thin film flow of a suspension of negatively buoyant particles down an incline. When the particle concentration is above a critical value, singular shock solutions can occur. We analyze the Hugoniot topology associated with the Riemann problem for this system, describing in detail how the transition from a double shock to a singular shock happens. We also derive the singular shock speed based on a key observation that the particles pile up at the maximum packing fraction near the contact line.

Key words. thin film, Riemann problem, conservation laws, singular shock

AMS subject classifications. 35L65 35L67 74K35

1. Introduction. The flow of thin viscous suspension with particles has important application in science and industry, such as the Bostwick consistometer in the food industry [21] and spiral separator in the mining industry [18]. However, a continuum description is complicated by the interplay of different physical effects including the increase of viscosity in the presence of particles [32, 4], the settling of heavy particles due to gravity [12], and particle resuspension induced by shear [19, 1]. Only recent studies have centered on particle-laden thin films down an incline with a free surface and moving contact lines.

Zhou et al. [34] first derived a theory for shock dynamics by considering a gravity-driven film of a dense suspension of glass beads in oil with conserved volume. Three different regimes were observed depending on the inclination angle and initial particle concentration. At low inclination angles and concentrations, particles settle out of the flow leading to the stratification of the suspension with a clear fluid moving ahead of the particles; at intermediate angles and concentrations, the suspension stays well-mixed; and at high concentrations and inclination angles the particles concentrate at the contact line to form a particle-rich ridge. To model the problem, they treat the mixture as a Newtonian flow locally, and describe the two-phase flow by a depth-average velocity depending on the effective viscosity of the suspension together with a relative velocity coming from the hindered settling. Shock solutions are obtained, however, the classical solution might cease to exist if the precursor thickness is smaller than a critical value. Cook et al. [8] revisited this model with a more complete explanation and more thorough characterization of the shock solutions. A singular shock is expected without further analysis, and they observe that for this singular shock, the particle concentration exceeds the limit of the close packing, making the model invalid in high concentrations. Cook [7] later developed a model to identify a balance between hindered settling and shear-induced migration as the leading order physics for particle-liquid separation.

Intensive experiments were carried out in [31] and [22]. In [31], Ward et. al stressed the gravitation effects in the flow with conserved volume. The average front position is found to obey the power law predicted for a clear fluid by Huppert [13] at

*This work was supported by UC Lab Fees Research Grant 09-LR-04-116741-BERA and NSF grant DMS-1312543.

†UCLA Department of Mathematics, Los Angeles, CA 90095 (liwang@math.ucla.edu).

‡UCLA Department of Mathematics, Los Angeles, CA 90095(bertozzi@math.ucla.edu).

moderate concentrations and deviation is observed when the concentration nears the maximum packing fraction. Murisic et al. [22] carried out experiments at different inclination angles and particle sizes showing that the equilibrium model in [7] explains the different settling regimes.

The work of Murisic et.al. [23] systematically derives a dynamic lubrication model for the flow building on the equilibrium theory [7, 22], and they also provide a careful quantitative comparison between the lubrication model and experiments in the settled regime. More details about shock structure in this regime are given in [20]. To date, the model has not been compared with experiments in the particle-rich ridge regime and this is in-part due to the more complicated dynamics of the model involving singular shocks. Our goal is to provide a detailed mathematical foundation for the model – focusing on this regime in which higher particle concentrations occur. The equilibrium model for particle settling has an unstable critical value for the concentration and we consider the case when the concentration is above this value so as to fall into the ridged regime. In this regime, three kinds of shocks form depending on the thickness and concentration of the precursor, two of which corresponds to the particle-rich ridge observed in the experiment, one is a singular shock and the other is double shock with intermediate height greater than the left and right heights. The thickness and concentration of the precursor play a major role in determining which solution is applicable. When the precursor is thinner than a threshold, only the singular shock exists; on the other hand a double shock solution exits for a thicker precursor. A third kind of shock solution is also relevant, it consists of a double shock with the intermediate state having almost zero concentration, more like the clear fluid observed in the settled regime.

Singular shocks were first studied by Keyfitz and Kranzer on a 2×2 strictly hyperbolic and genuinely nonlinear system [14, 16]. Based on a Dafermos regularization [9, 10], they derived a generalized Rankine-Hugoniot condition showing that mass concentration occurs in one variable only, providing a way to predict the shock speed. A rigorous derivation is given in [15] by constructing three sequences of approximating solutions and showing that they converge in the space of measures to a limit involving Dirac-like masses superimposed on a classical shock. Some numerics are carried out later to further understand the local structure of the singular shocks for this system [25]. Another famous system is the pressureless gas equations describing sticky particles, which admits delta shocks. There is a rich literature on the existence and local structure of these solutions [3, 5, 6, 30]. Some theoretical work exists on more general systems with restrictions [29, 28, 11, 24, 33, 26].

Our system, however, does not fall into any categories studied above. And the absence of the closed form for the flux functions further complicates the analysis. Rather, the flux functions are determined from the solutions of an ODE system. The formation of the singular shock in our case is very different from the Keyfitz-Kranzer system or the one in [8] which models the same phenomenon. Here the Hugoniot loci could extend to infinity but still fail to produce a physical intersection because the loci are *asymptotically parallel* in the far field. This also explains a special transition from a double shock to a singular shock, namely, the two speeds for the double shock become closer, while the intermediate state approaches infinity, until they coincide at a transition to the singular shock.

The rest of the paper is organized as follows. In the next section, we briefly review the model and prove rigorously some basic properties that have been observed experimentally and numerically in the prior papers. Then we focus on the case when

the particle concentration for the precursor is the same as bulk flow, with the results gathered in Section 3 and 4. Section 3 analyzes the classical single and double shock solution. Section 4 studies the origin and local structure of the singular shock, as well as its transition from the double shock. The results are extended in Section 5 to a more general case when the precursor has a different concentration from the bulk flow. At last, some concluding remarks are given in Section 6.

2. The Model. We first summarize the model in [23] for a thin-film flow of a well-mixed mixture of particles and liquid down an incline. The particles are assumed to be spherical monodisperse, non-colloidal, negatively buoyant and rigid while the liquid is incompressible. We assume the flow is transverse (y-direction) symmetric, so only the direction x along the substrate and normal direction z will be considered (see figure 2.1). The substrate is tilted an angle α to the horizontal. The particle volume fraction $0 \leq \phi(t,x,z) < 1$ and volume-averaged velocity $\mathbf{u}(t,x,z) = (u(t,x,z), w(t,x,z))$ are defined at every point (x,z) and time t. The mass density of particles and liquid satisfy $\rho_p > \rho_l$, where the subscript p and l represent *particle* and *liquid* from now on. The volume fraction ϕ does not exceed the maximum packing fraction ϕ_{max}. This was empirically measured to be $\phi_{max} = 0.61$ in the experiments in [23].

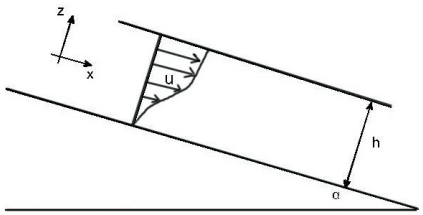

FIG. 2.1. *Sketches of the setup.*

Let $h(t,x)$ be the free surface, then $0 < z < h(t,x)$ and the governing equations are the Stokes' equations for the incompressible suspension and a conservation law for the particle volume:

$$\begin{cases} -\nabla \cdot \mathbf{\Pi} = (\rho_p \phi + (1-\phi)\rho_l)\,\mathbf{g}, & \text{(2.1a)} \\ \partial_t \phi + \mathbf{u} \cdot \nabla \phi + \nabla \cdot \mathbf{J} = 0, & \text{(2.1b)} \\ \nabla \cdot \mathbf{u} = 0, & \text{(2.1c)} \end{cases}$$

where $\mathbf{\Pi} = -p\mathbf{I} + \mu(\phi)\left(\nabla \mathbf{u} + \nabla \mathbf{u}^T\right)$ is the stress tensor, $\mu(\phi)$ is the effective suspension viscosity satisfying the Krieger-Dougherty relation [32, 4]:

$$\mu(\phi) = \mu_l (1 - \phi/\phi_{max})^{-2}. \tag{2.2}$$

The particle flux $\mathbf{J}$ takes the form

$$\mathbf{J} = \frac{d^2 \phi(\rho_p - \rho_l)}{18\mu_l} f_s(\phi)\mathbf{g} - \frac{d^2 K_c \phi}{4} \nabla\left(\dot{\gamma}\phi\right) - \frac{d^2 K_v \phi^2 \dot{\gamma}}{4\mu(\phi)} \frac{d\mu(\phi)}{d\phi} \nabla\phi,$$

where d is the particle diameter, and $\dot{\gamma} \approx \frac{\partial u}{\partial z}$ is the shear rate. The first term describes the hindered settling of particles due to gravity with hindrance function $f_s(\phi) = (1-\phi)/\mu(\phi)$, the second and the third terms refer to the shear-induced

migration as a result of particle collision and viscosity gradient respectively. Here $K_c = 0.41$ and $K_v = 0.62$ are empirical constants. The boundary conditions are: no-slip condition at the solid substrate $\mathbf{u}\big|_{z=0} = 0$, zero-stress condition at free surface $\mathbf{t}\cdot\mathbf{\Pi}\cdot\mathbf{n}\big|_{z=h} = 0$, zero-flux condition at both interfaces $\mathbf{J}\cdot\mathbf{n}\big|_{z=0} = \mathbf{J}\cdot\mathbf{n}\big|_{z=h} = 0$, and kinematic boundary condition at the free surface $\partial_t h = w - u\partial_x h\big|_{z=h}$. Here $\mathbf{n}$ is the outward normal unit vector.

We rescale system (2.1) in the same spirit as in the lubrication theory with two parameters $\epsilon = \frac{[z]}{[x]}$ and $\eta = \frac{d}{[z]}$. Under the continuum assumption and the assumption that the particle flux in z-direction is in equilibrium, we require $\epsilon \ll \eta^2 \ll 1$. Then a formal asymptotic expansion leads to the evolution equations for h and ϕ [23]. The leading order equations of (2.1b) and (2.1a) give rise to the following equilibrium model for particle settling:

$$\begin{cases} \left(1 + C_1\dfrac{\tilde{\phi}}{\phi_{max}-\tilde{\phi}}\right)\tilde{\sigma}\tilde{\phi}' + C_2 - (C_2+1)\tilde{\phi} - \rho_s\tilde{\phi}^2 = 0, \quad 0 < \tilde{\phi} < \phi_{max}, & \text{(2.3a)} \\ \tilde{\sigma}' = -(1+\rho_s\tilde{\phi}), & \text{(2.3b)} \\ \tilde{\sigma}(1) = 0, & \text{(2.3c)} \\ \tilde{\sigma}(0) = 1 + \rho_s\phi_0(t,x), & \text{(2.3d)} \end{cases}$$

where the stress $\tilde{\sigma}$ is defined as $\tilde{\sigma} = \mu(\tilde{\phi})\tilde{u}'$. Since the equilibrium equations are independent of the axial flow and time, we introduce a new variable $s = \frac{z}{h(t,x)}$ with $0 \le s \le 1$ so as to get rid of the implicit dependence on $h(t,x)$. The tilde here indicates the quantities using the s scaling, and all primes in (2.3) are derivatives in s. Whenever $\tilde{\phi}(t,x;s) = 0$ or $\tilde{\phi}(t,x;s) = \phi_{max}$, (2.3a) is replaced by $\tilde{\phi}' = 0$ so as to describe the clear fluid or packed particles. $C_1 = \frac{2(K_v - K_c)}{K_c}$, $C_2 = \frac{2\rho_s \cot\alpha}{9K_c}$, $\rho_s = \frac{\rho_p - \rho_l}{\rho_l}$ are three constants. ϕ_0 is the z-averaged particle volume fraction

$$\phi_0(t,x) = \int_0^1 \tilde{\phi}(t,x;s)ds \in [0, \phi_{max}], \tag{2.4}$$

and the solution of the ODE system (2.3) has ϕ_0 as a parameter. The velocity $\tilde{u}(t,x;s)$ solves the equation

$$\tilde{u}'(t,x;s) = \frac{\tilde{\sigma}(t,x;s)}{\mu(\tilde{\phi}(t,x;s))}, \qquad \tilde{u}(t,x;0) = 0. \tag{2.5}$$

The next order terms lead to the evolution equations for $h(t,x)$ and $n(t,x) \equiv \phi_0(t,x)h(t,x)$:

$$\begin{cases} \partial_t h + \partial_x\left(h^3\displaystyle\int_0^1 \tilde{u}(t,x;s)ds\right) = 0, & \text{(2.6a)} \\ \partial_t n + \partial_x\left(h^3\displaystyle\int_0^1 \tilde{\phi}(t,x;s)\tilde{u}(t,x;s)ds\right) = 0, & \text{(2.6b)} \end{cases}$$

satisfying the conservation of particle volume and total volume of the suspension respectively. Written in a more compact form, let

$$f(\phi_0) = \int_0^1 \tilde{u}(t,x;s)ds, \quad g(\phi_0) = \int_0^1 \tilde{\phi}(t,x;s)\tilde{u}(t,x;s)ds, \tag{2.7}$$

then we have

$$h_t + \left(h^3 f\left(\frac{n}{h}\right)\right)_x = 0, \quad n_t + \left(h^3 g\left(\frac{n}{h}\right)\right)_x = 0, \tag{2.8}$$

and the Jacobian matrix of this system is

$$J = h^2 \begin{pmatrix} 3f - \phi_0 f' & f' \\ 3g - \phi_0 g' & g' \end{pmatrix}, \tag{2.9}$$

where the derivatives of f and g are with respect to ϕ_0. This system is strictly hyperbolic as explained in [23]. Here we plot the discriminant of the Jacobian matrix in (2.9)

$$\mathcal{D} = (3f - \phi_0 f' + g')^2 - 12(fg' - f'g) \tag{2.10}$$

versus ϕ_0 for different angles in Figure 2.2, where $\mathcal{D} > 0$ guarantees the hyperbolicity of the system.

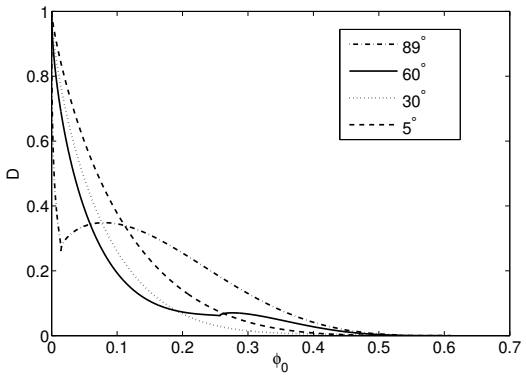

FIG. 2.2. *The discriminant $\mathcal{D}$ of (2.10) versus ϕ_0 for different angles, shown in the legend.*

2.1. The equilibrium model for particle settling. In this section, we explore some properties of the solutions to (2.3). The first result is as follows, which was observed numerically in [22] and experimentally in [31], and here we present a rigorous proof.

THEOREM 2.1. *Consider a solution $\tilde{\phi}(t, x; s)$ of equations (2.3) with $0 \le s < 1$. Let $\phi_{crit} \in [0, \phi_{max}]$ be the critical point that solves $\rho_s \tilde{\phi}^2 + (C_2 + 1)\tilde{\phi} - C_2 = 0$.*

If $\phi_{max} > \tilde{\phi}(t, x; 0) > \phi_{crit}$, then $\tilde{\phi}(t, x; s)$ is monotonically non-decreasing with respect to s and $\phi_0 > \phi_{crit}$;

If $0 < \tilde{\phi}(t, x; 0) < \phi_{crit}$, then $\tilde{\phi}(t, x; s)$ is monotonically non-increasing with respect to s and $\phi_0 < \phi_{crit}$. Therefore, ϕ_{crit} is unstable.

Proof. In this proof, we omit the dependence on (t, x) without ambiguity. For the system (2.3), first notice that the solution $\tilde{\phi}(s)$ to (2.3a) is in $(0, \phi_{max})$, so $\tilde{\sigma}(s)$ is monotone decreasing according to (2.3b). And since $\tilde{\sigma}(1) = 0$, we have $\tilde{\sigma}(s) > 0$ for $0 \le s < 1$. Let $A(\tilde{\phi}) = 1 + C_1 \frac{\tilde{\phi}}{\phi_{max} - \tilde{\phi}}$ and $B(\tilde{\phi}) = (C_2 + 1)\tilde{\phi} + \rho_s \tilde{\phi}^2 - C_2$, write (2.3a) as $\tilde{\sigma} A(\tilde{\phi})\tilde{\phi}'(s) = B(\tilde{\phi})$, then one has $\tilde{\sigma} A(\tilde{\phi}) \left(\tilde{\phi} - \phi_{crit}\right)'(s) = B(\tilde{\phi}) - B(\phi_{crit}) = B'(\xi(\tilde{\phi})) \left(\tilde{\phi} - \phi_{crit}\right)(s)$, where $\xi(\tilde{\phi})$ is between ϕ_{crit} and $\tilde{\phi}(s)$. Written in a more

explicit form yields $\tilde{\phi}(s)-\phi_{crit}=\left(\tilde{\phi}-\phi_{crit}\right)(0)\exp\left\{\int_0^s \frac{B'\left(\xi\left(\tilde{\phi}(\tau)\right)\right)}{A(\tilde{\phi}(s))\tilde{\sigma}(\tau)}d\tau\right\}$. Therefore, if $\tilde{\phi}(0)>\phi_{crit}$, $\tilde{\phi}(s)>\phi_{crit}$ for all $0<s<1$ and thus $\phi_0>\phi_{crit}$. Since $B(\tilde{\phi}(s))>0$ for $\tilde{\phi}(s)>\phi_{crit}$, $\tilde{\phi}'(s)\geq 0$ in this case. The other case when $\tilde{\phi}(0)<\phi_{crit}$ can be carried out in the same manner. □

The theorem implies that the well-mixed state where $\phi_0\equiv\phi_{crit}$ is unstable and will bifurcate into either ridged case or settled case. Figure 2.3 displays the profiles of $\tilde{\phi}$, $\tilde{u}$ and $\tilde{\sigma}$ when the inclination angle is 30°.

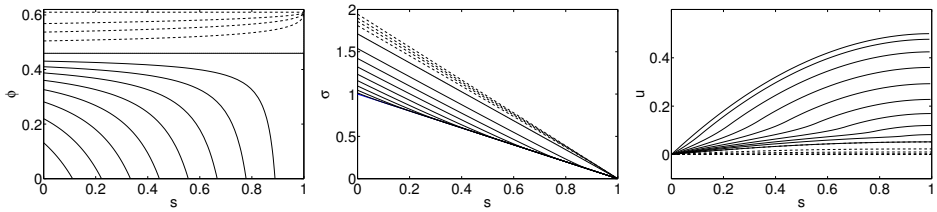

FIG. 2.3. *Plots of the solutions to (2.3) for angle = 30°. The x-axis is s. Different curves refer to different initial data ϕ_0 with solid line representing $\phi_0<\phi_{crit}$ and dashed line $\phi_0>\phi_{crit}$. Left: particle volume fraction $\tilde{\phi}$, Middle: shear stress $\tilde{\sigma}$, Right: suspension velocity $\tilde{u}$.*

THEOREM 2.2. *The fluxes $f(\phi_0)$ and $g(\phi_0)$ defined in* (2.7) *satisfy: if $\phi_0>\phi_{crit}$, then $g(\phi_0)\geq f(\phi_0)\phi_0$; if $\phi_0<\phi_{crit}$, then $g(\phi_0)\leq f(\phi_0)\phi_0$.*

This theorem says that when $\phi_0>\phi_{crit}$, the average particle velocity exceeds the average suspension velocity, corresponding to the ridged regime. And the case $\phi_0<\phi_{crit}$ corresponds to the settled regime since the average particle velocity is less than the suspension velocity.

Proof. First notice that $\tilde{u}(s)$ is a monotone increasing function in s because of (2.5). Then

$$g(\phi_0)-\phi_0 f(\phi_0)=\int_0^1\tilde{\phi}(s)\tilde{u}(s)ds-\phi_0\int_0^1\tilde{u}(s)ds=\int_0^1\left(\tilde{\phi}(s)-\phi_0\right)\tilde{u}(s)ds.$$

From Theorem 2.1, one sees that when $\phi_0>\phi_{crit}$, $\tilde{\phi}(s)$ is monotone non-decreasing, thus $\exists\, a\in(0,1)$ such that $\tilde{\phi}(s)\leq\phi_0$ when $s\leq a$ and $\tilde{\phi}(s)\geq\phi_0$ when $s\geq a$. Therefore

$$\begin{aligned}\int_0^1\left(\tilde{\phi}(s)-\phi_0\right)\tilde{u}(s)ds&=\int_0^a\left(\tilde{\phi}(s)-\phi_0\right)\tilde{u}(s)ds+\int_a^1\left(\tilde{\phi}(s)-\phi_0\right)\tilde{u}(s)ds\\&=\left[\int_0^a\left(\tilde{\phi}(s)-\phi_0\right)\frac{\tilde{u}(s)}{\tilde{u}(a)}ds+\int_a^1\left(\tilde{\phi}(s)-\phi_0\right)\frac{\tilde{u}(s)}{\tilde{u}(a)}ds\right]\tilde{u}(a)\\&\geq\left[\int_0^a\left(\tilde{\phi}(s)-\phi_0\right)ds+\int_a^1\left(\tilde{\phi}(s)-\phi_0\right)ds\right]\tilde{u}(a)=0,\end{aligned}$$

where we use the fact that $\frac{\tilde{u}(s)}{\tilde{u}(a)}\leq 1$ for $0\leq s\leq a$ and $\frac{\tilde{u}(s)}{\tilde{u}(a)}\geq 1$ for $1\geq s\geq a$. When $\phi_0<\phi_{crit}$, the result can be derived *mutatis mutandis.* □

REMARK 2.3. *From the previous two theorems, we note that $g(\phi_{crit})=\phi_{crit}f(\phi_{crit})$, which can be further observed in Figure 2.4.*

3. Classical shock solutions for $\phi_R=\phi_L$. In this and the following sections, we concentrate on the hyperbolic system (2.8) with Riemann initial data

$$h(0,x)=\begin{cases}h_L & x<0\\ h_R & x>0\end{cases},\phi_0(0,x)=\begin{cases}\phi_L & x<0\\ \phi_R & x>0\end{cases},n(0,x)=h(0,x)\phi_0(0,x),\quad(3.1)$$

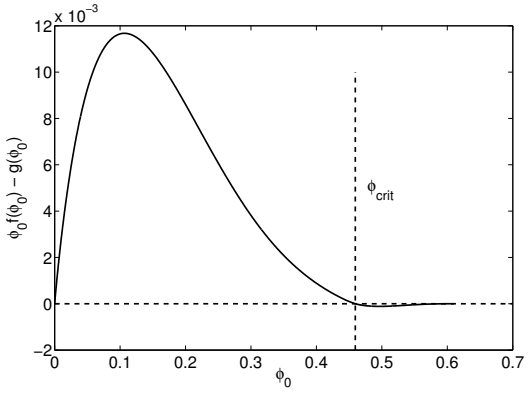

FIG. 2.4. *Plot of $f(\phi_0)\phi_0 - g(\phi_0)$ versus ϕ_0 for the angle* $=30°$.

where h_L and ϕ_L denote the height of the mixture and particle concentration for the reservoir, while h_R and ϕ_R refer to the precursor correspondingly. For now we focus on the case $\phi_R = \phi_L$ as in [8] corresponding to the same particle concentration in the reservoir being used to prewet the substrate. Later we consider the role of a variable ϕ_R.

3.1. Single shock solution. Here we summarize the result for the critical case $\phi_L = \phi_R = \phi_{crit}$, where a classical single shock solution is obtained. This corresponds to the *well-mixed* regime where the particles and liquid flow along the substrate at the same speed.

PROPOSITION 3.1. *The solution to the Riemann problem (2.3) (2.8) (3.1) with* $\phi_0(0,x) = \phi_L = \phi_R = \phi_{crit}$ *is*

$$h(t,x) = \begin{cases} h_L & x < st \\ h_R & x > st \end{cases}, \quad n(t,x) = h(t,x)\phi_{crit}, \tag{3.2}$$

where $s = f(\phi_{crit})\frac{h_R^3 - h_L^3}{h_R - h_L}$, *and satisfies the entropy condition* $\lambda_L^{(2)} > s > \lambda_R^{(2)}$. *Here* $\lambda_{L/R}^{(2)}$ *are the 2-characteristic speeds for the left and right states respectively.*

For a general 2×2 system, a classical solution of the Riemann problem has the form of a double wave structure [17]. However, for this special choice of left and right states, there is a single 2-shock.

Proof. Notice $g(\phi_{crit}) = \phi_{crit} f(\phi_{crit})$, so the left and right states satisfy the Rankine-Hugoniot jump conditions

$$s = \frac{h_R^3 - h_L^3}{h_R - h_L} f(\phi_{crit}) = \frac{h_R^3 - h_L^3}{(h_R - h_L)\phi_{crit}} g(\phi_{crit}). \tag{3.3}$$

Since $\tilde{\phi}(s;\phi_{crit}) = \phi_{crit}$ by (2.3a), we have $\tilde{\sigma}(s;\phi_{crit}) = (1-s)(1+\rho_s\phi_{crit})$, which leads to

$$\tilde{u}(s;\phi_{crit}) = \left(s - \frac{1}{2}s^2\right)\frac{1+\rho_s\phi_{crit}}{\mu_l}\left(1 - \frac{\phi_{crit}}{\phi_{max}}\right)^2 = A\left(s - \frac{1}{2}s^2\right).$$

Then from (2.7), one sees that

$$g'(\phi_{crit}) - f'(\phi_{crit})\phi_{crit} = \int_0^1 \Big[\tilde{u}_{\phi_0}(s;\phi_{crit})\tilde{\phi}(s;\phi_{crit}) + \tilde{u}(s;\phi_{crit})\tilde{\phi}_{\phi_0}(s;\phi_{crit}) - \phi_{crit}\tilde{u}_{\phi_0}(s;\phi_{crit})\Big]\, ds$$
$$= \int_0^1 \tilde{u}(s;\phi_{crit})\tilde{\phi}_{\phi_0}(s;\phi_{crit})ds = \int_0^1 A\left(s - \frac{1}{2}s^2\right)\tilde{\phi}_{\phi_0}(s;\phi_{crit})ds.$$

Notice $\int_0^1 \tilde{\phi}(s;\phi_0)ds = \phi_0,\ \forall \phi_0 \in [0,\phi_{max}]$, one has $\int_0^1 \tilde{\phi}_{\phi_0}(s;\phi_{crit})ds = 1$. From (2.3a), it is not hard to see that $\tilde{\phi}_{\phi_0}(s;\phi_{crit}) \geq 0$ for all $s \in [0,1]$. Thus we have,

$$g'(\phi_{crit}) - f'(\phi_{crit})\phi_{crit} \leq A \max_{s\in[0,1]}\left(s - \frac{1}{2}s^2\right)\int_0^1 \tilde{\phi}_{\phi_0}(s;\phi_{crit})ds = \frac{A}{2}$$
$$< 3\int_0^1 \tilde{u}(s;\phi_{crit})ds = 3f(\phi_{crit}).$$

Therefore, the two eigenvalues of the flux matrix (2.9) when $\phi_0 = \phi_{crit}$ are

$$\lambda^{(1)}_{L/R} = h^2_{L/R}\left(g'(\phi_{crit}) - \phi_{crit}f'(\phi_{crit})\right),\ \lambda^{(2)}_{L/R} = 3h^2_{L/R}f(\phi_{crit}).$$

And the entropy condition $\lambda^{(2)}_L > s = \left(h_L^2 + h_L h_R + h_R^2\right) f(\phi_{crit}) > \lambda^{(2)}_R$ immediately follows. □

3.2. Double shock solution. Throughout this section, we assume $\phi_L > \phi_{crit}$, and fix $h_L = 1$ for all the numerical experiments from now on without loss of generality. When $\phi_R = \phi_L$, and the precursor $h_R \gg 0$, we find a double shock solution with intermediate state h_M higher than h_L and h_R. The other case when $\phi_R \ll \phi_L$ induces another kind of double shock with ϕ_M much smaller than $\phi_L(\phi_R)$, which is more like a clear fluid that appears in the settled case, and we will discuss it in more detail in Section 5.

Given a left state (h_L, ϕ_L), we can draw a curve which contains all the states (h, ϕ_0) that connect to it by a discontinuity satisfying the jump condition:

$$\frac{h^3 f(\phi_0) - h_L^3 f(\phi_L)}{h - h_L} = \frac{h^3 g(\phi_0) - h_L^3 g(\phi_L)}{h\phi_0 - h_L\phi_L}. \tag{3.4}$$

The set of all points on this curve is called the Hugoniot locus for (h_L, ϕ_L). However, not all points are physically *admissible* as they do not satisfy the entropy condition. We plot the admissible part of the Hugoniot locus for (h_L, ϕ_L) in figure 3.1 on the left using black and grey dots. Here the black dots represent the states that connect to the left state through a 1-shock satisfying:

$$\lambda^{(1)}(h_L,\phi_L) > s_1 > \lambda^{(1)}(h,\phi_0),\ \ s_1 < \lambda^{(2)}(h,\phi_0); \tag{3.5}$$

and the grey dots refer to the states that connect to the left state through a 2-shock satisfying:

$$\lambda^{(2)}(h_L,\phi_L) > s_2 > \lambda^{(2)}(h,\phi_0),\ \ s_2 > \lambda^{(1)}(h_L,\phi_L), \tag{3.6}$$

where s_1 and s_2 are shock speeds calculated by the jump condition, $\lambda^{(i)}$, $i = 1, 2$ are the eigenvalues of (2.8). The admissible part of the Hugoniot locus for a given

right state (h_R, ϕ_R) is also drawn in figure 3.1 with pluses. Here the black pluses correspond to the states that connect to the right state through 1-shock satisfying

$$\lambda^{(1)}(h, \phi_0) > s_1 > \lambda^{(1)}(h_R, \phi_R), \quad s_1 < \lambda^{(2)}(h_R, \phi_R); \tag{3.7}$$

and the grey pluses represent the states that connect to the right states through 2-shock satisfying

$$\lambda^{(2)}(h, \phi_0) > s_2 > \lambda^{(2)}(h_R, \phi_R), \quad s_2 > \lambda^{(1)}(h, \phi_0). \tag{3.8}$$

Therefore, the intersection of the locus of black dots and the locus of grey pluses is the admissible intermediate state that connect the left state through a 1-shock and right state through a 2-shock.

Figure 3.1 on the right presents the Riemann solution obtained by numerically solving (2.8), where the double shock is observed, although the 1-shock is not sharp due to numerical diffusion. The intermediate state is found to be $(h_M, n_M) = (1.3137, 0.6978)$, which matches the intersection point for the Hugoniot loci on the left.

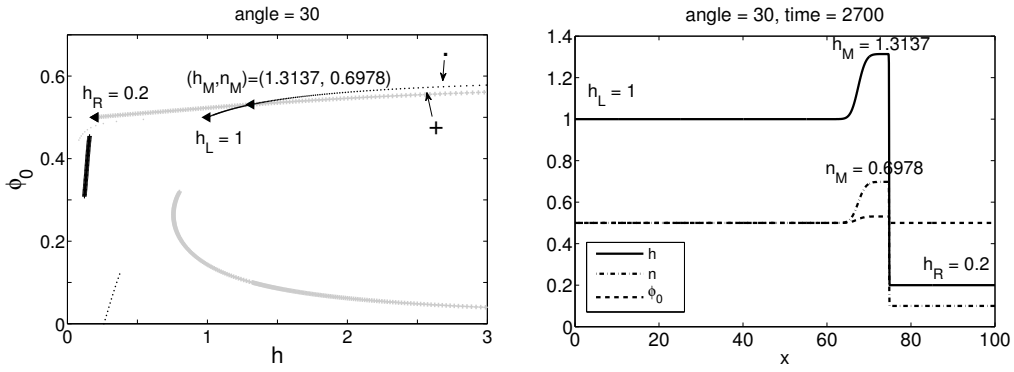

FIG. 3.1. *Left: the Hugoniot loci for the left state* $(h_L, \phi_L) = (1, 0.5)$ *and the right state* $(h_R, \phi_R) = (0.2, 0.5)$. *The 'dot' represents the* admissible *shocks connecting to the left state while 'plus' represents the ones connecting to the right state. Black refers to the 1-shock and grey refers to the 2-shock. Right: the Riemann solution for* (2.8) *with above initial condition.*

The time evolution of double-shock is fairly interesting. As displayed in figure 3.2, this happens for any intermediate state that is higher than the left and right states, but after a while this state stops growing higher but begins to expand to form a double shock.

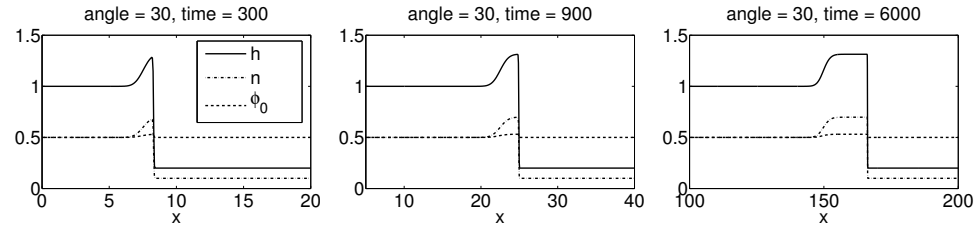

FIG. 3.2. *The profiles of* h, n, *and* ϕ_0 *for different times with initial data* $(h_L, \phi_L) = (1, 0.5)$ *and* $(h_R, \phi_R) = (0.2, 0.5)$ *for angle* $= 30°$.

4. Singular shock solution for $\phi_R = \phi_L$. When the precursor h_R is small, a singular shock forms: the intermediate height in the shock layer grows without bound while the value of ϕ approaches ϕ_{max}. This singularity is not directly observed in the experiment because surface tension and the normal component of gravity will smooth this effect. But experimental observations show that the particles in the front pile up with a high concentration that may be well described by a singular shock, to leading order. This is one of the few examples of singular shocks that one might observe in a physical experiment. Future experiments might compare the speed of the front with the speed predicted by the singular theory.

4.1. Formation of the singular shock. For the Keyfitz-Kranzer system, which is strictly hyperbolic and genuinely nonlinear, the Hugoniot locus is a closed figure-eight shaped curve, and thus fails to produce a classical shock if two initial states are not close [14, 15, 16]. In Cook et al.'s model [8], a similar topology of the Hugoniot locus again leads to the singular shock. However, in this new model (2.3)–(2.6), the mechanism for the generation of singular shock is quite different.

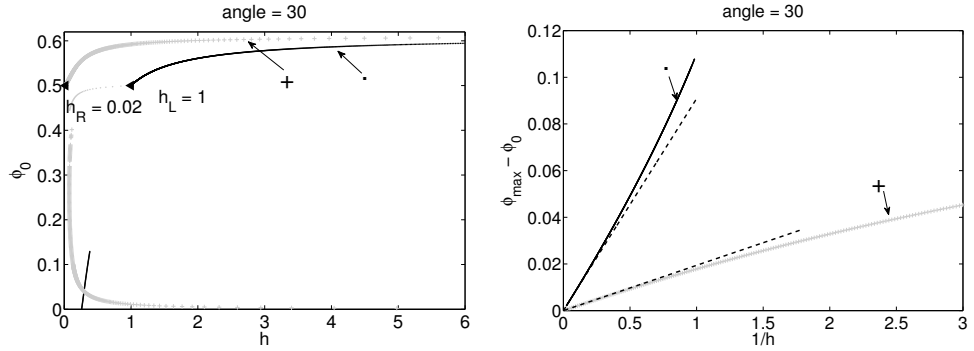

FIG. 4.1. *Left: the admissible shocks connecting the left state $(h_L, \phi_L) = (1, 0.5)$ (dots) and right state $(h_R, \phi_R) = (0.02, 0.5)$ (pluses). Right: the re-plot of the two Hugoniot loci on the left with y-axis representing $\phi_{max} - \phi_0$ and x-axis representing $\frac{1}{h}$. The dashed lines are the leading order asymptotics calculated using formulas (4.4) and (4.5).*

We start with figure 4.1. On the left we have the Hugoniot loci connecting to left state $(h_L, \phi_L) = (1, 0.5)$ and right state $(h_R, \phi_R) = (0.02, 0.5)$. Similar to figure 3.1, the dots represent the *admissible* shocks connecting to the left states while the pluses represent the ones connecting to the right states. Black refers to the 1-shock and grey refers to the 2-shock. So we look for an intersection of the black dots and the grey pluses. First the lower intersection in figure 4.1 is discarded because the shock speed for the 1-wave is faster than the 2-wave. We then turn our attention to the region $\phi_0 > \phi_{crit}$. Here both the black dots and grey plus are increasing and approaching $\phi = \phi_{max}$. In order to see whether they will intersect at large values of h, figure 4.1 on the right gives a plot of $\phi_{max} - \phi_0$ versus $\frac{1}{h}$, where the slope of the grey curve near zero is smaller than black one, which means the grey one will stay above black one when $h \to \infty$, and thus produces no intersection. To further check it analytically, we take a closer look at the asymptotic behavior of both curves when h is large. The following result emphasizes one of the main themes of this paper.

THEOREM 4.1. *Assume $\phi_L = \phi_R$ and we use ϕ_L and ϕ_R interchangeable in this section. Let $(h, \phi_0 = \Phi_R(h, \phi_R, h_R))$ denote the admissible 2-shock connecting to the right state (h_R, ϕ_R) (i.e. the grey pluses in figure 4.1) with $h > h_R$, and*

$(h, \phi_0 = \Phi_L(h, \phi_L, h_L))$ denote the admissible 1-shock connecting to the left state (h_L, ϕ_L) (i.e. the black dots in figure 4.1) with $h > h_L$, then we have

$$\lim_{h\to\infty} \Phi_R(h, \phi_R, h_R) = \lim_{h\to\infty} \Phi_L(h, \phi_L, h_L) = \phi_{max}. \tag{4.1}$$

Moreover, when h is large, one has

$$\phi_{max} - \Phi_L(h, \phi_L, h_L) \sim C_L(\phi_L)\frac{h_L}{h} + o\left(\frac{1}{h}\right), \tag{4.2}$$

$$\phi_{max} - \Phi_R(h, \phi_R, h_R) \sim C_R(\phi_L)\frac{h_R}{h} + o\left(\frac{1}{h}\right), \tag{4.3}$$

where

$$C_L(\phi_L) = (\phi_{max} - \phi_L)\,\frac{1+B}{B}\left(1 - \cos\frac{\theta}{3} + \sqrt{3}\sin\frac{\theta}{3}\right), \tag{4.4}$$

$$C_R(\phi_L) = (\phi_{max} - \phi_L)\,\frac{1+B}{B}\left(1 + 2\cos\frac{\theta}{3}\right), \tag{4.5}$$

and

$$B = \frac{\rho_s\phi_{max}^2 + (C_2+1)\phi_{max} - C_2}{C_1\phi_{max}(1+\rho_s\phi_{max})}, \tag{4.6}$$

$$\theta = \arccos\left(1 + \frac{3B^2(2B+3)\phi_{max}^2\mu_l}{2(\phi_{max}-\phi_L)^3(1+\rho_s\phi_{max})(1+B)^4}\left(g(\phi_L) - \phi_{max}f(\phi_L)\right)\right). \tag{4.7}$$

As an immediate consequence of the above theorem and figure 4.1, we have the threshold value h_R^* defined as

$$h_R^* = h_L\frac{C_L(\phi_L)}{C_R(\phi_L)} = h_L\frac{1 - \cos\frac{\theta}{3} + \sqrt{3}\sin\frac{\theta}{3}}{1 + 2\cos\frac{\theta}{3}}, \tag{4.8}$$

where θ is defined in (4.7). Then if $h_R > h_R^*$, the Hugoniot loci will intersect at (h_M, ϕ_M) with $h_M > \max(h_L, h_R)$, leading to a double shock. If $h_R = h_R^*$, the Hugoniot loci are tangent at $\frac{1}{h} = 0$, and if $h_R < h_R^*$ they will not intersect, both cases lead to a singular shock.

Next, we present the following two lemmas required for the proof of Theorem 4.1.

Lemma 4.2.

$$\tilde{\phi}_{\phi_0}(s;\phi_0)\Big|_{\phi_0=\phi_{max}} = (1+B)(1-s)^B, \tag{4.9}$$

where B is defined in (4.6).

Proof. Recall the equation (2.3a) for $\tilde{\phi}$, one has

$$\tilde{\phi}'_{\phi_0}(s;\phi_0) = \left[\frac{\rho_s\tilde{\phi}^2 + (C_2+1)\tilde{\phi} - C_2}{\left(\phi_{max} - \tilde{\phi} + C_1\tilde{\phi}\right)\tilde{\sigma}}\right]_{\phi_0}\left(\phi_{max} - \tilde{\phi}\right) - \frac{\rho_s\tilde{\phi}^2 + (C_2+1)\tilde{\phi} - C_2}{\left(\phi_{max} - \tilde{\phi} + C_1\tilde{\phi}\right)\tilde{\sigma}}\tilde{\phi}_{\phi_0},$$

therefore

$$\tilde{\phi}'_{\phi_0}(s;\phi_{max}) = -\frac{\rho_s\phi_{max}^2 + (C_2+1)\phi_{max} - C_2}{C_1\phi_{max}(1+\rho_s\phi_{max})(1-s)}\tilde{\phi}_{\phi_0} = -\frac{B}{1-s}\tilde{\phi}_{\phi_0}(s;\phi_{max}), \tag{4.10}$$

where we use the fact that $\tilde{\sigma}(s;\phi_{max}) = (1-s)(1+\rho_s\phi_{max})$ and $\tilde{\phi}(s;\phi_{max}) \equiv \phi_{max}$. Moreover, since $\int_0^1 \tilde{\phi}(s;\phi_0)ds = \phi_0$, $\forall \phi_0 \in [0,\phi_{max}]$ one sees

$$\int_0^1 \tilde{\phi}_{\phi_0}(s;\phi_{max})ds = 1. \tag{4.11}$$

Then (4.10) together with (4.11) as an ODE for $\tilde{\phi}_{\phi_0}(s;\phi_{max})$ readily implies (4.9). □

LEMMA 4.3. *The flux functions $f(\phi_0)$ and $g(\phi_0)$ at $\phi_0 = \phi_{max}$ satisfy*

$$f(\phi_{max}) = g(\phi_{max}) = 0, \tag{4.12}$$
$$\phi_{max} f'(\phi_{max}) = g'(\phi_{max}) = 0, \tag{4.13}$$
$$\phi_{max} f''(\phi_{max}) = g''(\phi_{max}) \neq 0. \tag{4.14}$$

Proof. First $\mu(\phi) = \mu_l(1-\phi/\phi_{max})^{-2}$ together with (2.5) implies $\tilde{u}(s;\phi_{max}) \equiv 0$, and thus indicates $f(\phi_{max}) = g(\phi_{max}) = 0$. For the first derivative, recall the definition of $f(\phi_0)$ and $g(\phi_0)$ in (2.7), one has

$$f'(\phi_0) = \int_0^1 \tilde{u}_{\phi_0}(s;\phi_0)ds, \;\; g'(\phi_0) = \int_0^1 \tilde{u}_{\phi_0}(s;\phi_0)\tilde{\phi}(s;\phi_0)ds + \int_0^1 \tilde{u}(s;\phi_0)\tilde{\phi}_{\phi_0}(s;\phi_0)ds.$$

Again $\tilde{\phi}(s;\phi_{max}) = \phi_{max}$ and $\tilde{u}(s;\phi_{max}) = 0$ lead to $\phi_{max}f'(\phi_{max}) = g'(\phi_{max})$. In fact, from (2.5), one sees that

$$\tilde{u}(s;\phi_0) = \int_0^s \frac{\tilde{\sigma}(\tau;\phi_0)}{\mu_l}\left(1 - \frac{\tilde{\phi}(\tau;\phi_0)}{\phi_{max}}\right)^2 d\tau, \tag{4.15}$$

then

$$\tilde{u}_{\phi_0}(s;\phi_{max}) = \frac{1}{\mu_l}\int_0^s \left\{ \tilde{\sigma}_{\phi_0}\left(1 - \frac{\tilde{\phi}}{\phi_{max}}\right)^2 - \frac{2\tilde{\sigma}}{\phi_{max}}\left(1 - \frac{\tilde{\phi}}{\phi_{max}}\right)\tilde{\phi}_{\phi_0} \right\} d\tau \Big|_{\phi_0=\phi_{max}} = 0,$$

which implies $f'(\phi_{max}) = g'(\phi_{max}) = 0$. The second derivative takes the form

$$\tilde{u}_{\phi_0\phi_0}(s;\phi_{max}) = \frac{1}{\mu_l}\int_0^s \frac{2}{\phi_{max}^2}\tilde{\sigma}(\tau;\phi_0)\left(\tilde{\phi}_{\phi_0}\right)^2 d\tau\Big|_{\phi_0=\phi_{max}} \neq 0, \tag{4.16}$$

where we have already discard the zero value terms when evaluated at $\phi_0 = \phi_{max}$ and the last inequality is obtained by Lemma 4.2. As a result, the second derivatives of the flux satisfy

$$\begin{aligned} f''(\phi_{max}) &= \int_0^1 \tilde{u}_{\phi_0\phi_0}(s;\phi_0)ds\Big|_{\phi_0=\phi_{max}} \neq 0, \\ g''(\phi_{max}) &= \int_0^1 \tilde{u}_{\phi_0\phi_0}\tilde{\phi}ds + 2\int_0^1 \tilde{u}_{\phi_0}\tilde{\phi}_{\phi_0}ds + \int_0^1 \tilde{u}\tilde{\phi}_{\phi_0\phi_0}ds\Big|_{\phi_0=\phi_{max}} \\ &= \phi_{max}\int_0^1 \tilde{u}_{\phi_0\phi_0}(s;\phi_0)ds\Big|_{\phi_0=\phi_{max}} = \phi_{max}f''(\phi_{max}). \end{aligned}$$

□

Proof. [Proof of Theorem 4.1.] The curve $\phi_0 = \Phi_L(h, \phi_L, h_L)$ solves (3.4), which reformulates to

$$\begin{aligned}\mathcal{F}(h,\phi_0) = &\big[\phi_0 f(\phi_0) - g(\phi_0)\big] + \frac{h_L}{h}\big[g(\phi_0) - f(\phi_0)\phi_L\big] \\ &+\frac{h_L^3}{h^3}\big[g(\phi_L) - f(\phi_L)\phi_0\big] + \frac{h_L^4}{h^4}\big[f(\phi_L)\phi_L - g(\phi_L)\big] = 0. \end{aligned} \tag{4.17}$$

Passing to the limit $h \to \infty$ yields $\phi_0 f(\phi_0) - g(\phi_0) = 0$, thus by Theorem 2.2 and (4.12), one has $\phi_0 = \phi_{max}$ in this limit. Denote $\phi_1 = \phi_0 - \phi_{max}$, inserting $\phi_0 = \phi_{max} + \phi_1$ into (4.17), expanding $f(\phi_0)$ and $g(\phi_0)$ by Taylor series and collecting the terms according to the orders of ϕ_1 lead to

$$\begin{aligned}&\phi_1\Big[\phi_{max}f'(\phi_{max}) - g'(\phi_{max})\Big] + \phi_1^2\Big[\frac{1}{2}\phi_{max}f''(\phi_{max}) + f'(\phi_{max}) - \frac{1}{2}g''(\phi_{max})\Big] \\ &+\frac{1}{6}\phi_1^3\Big[f'''(\phi_{max})\phi_{max} + 3f''(\phi_{max}) - g'''(\phi_{max})\Big] \\ &+\frac{1}{24}\phi_1^4\Big[f^{(4)}(\phi_{max})\phi_{max} + 4f'''(\phi_{max}) - g^{(4)}(\phi_{max})\Big] + \cdots \\ &+ \frac{h_L}{h}\Big[g'(\phi_{max}) - \phi_L f'(\phi_{max})\Big]\phi_1 + \frac{1}{2}\frac{h_L}{h}\Big[g''(\phi_{max}) - \phi_L f''(\phi_{max})\Big]\phi_1^2 + \\ &+\frac{1}{6}\frac{h_L}{h}\Big[g'''(\phi_{max}) - \phi_L f'''(\phi_{max})\Big]\phi_1^3 + \cdots \\ &+ \frac{h_L^3}{h^3}\Big[g(\phi_L) - f(\phi_L)\phi_{max}\Big] - \frac{h_L^3}{h^3}f(\phi_L)\phi_1 + \frac{h_L^4}{h^4}\Big[f(\phi_L)\phi_L - g(\phi_L)\Big] = 0. \end{aligned} \tag{4.18}$$

Then by Lemma 4.3, the first few terms vanish, and the terms at order $O(\phi_1^3)$, $O\left(\frac{\phi_1^2}{h}\right)$ and $O\Big(\frac{1}{h^3}\Big)$ solve

$$a\phi_1^3 + b\phi_1^2 + d = 0, \tag{4.19}$$

where

$$\begin{aligned} a &= \frac{1}{6}\left[f'''(\phi_{max})\phi_{max} + 3f''(\phi_{max}) - g'''(\phi_{max})\right], \\ b &= \frac{1}{2}\frac{h_L}{h}\left[g''(\phi_{max}) - \phi_L f''(\phi_{max})\right], \\ d &= \frac{h_L^3}{h^3}\left[g(\phi_L) - f(\phi_L)\phi_{max}\right]. \end{aligned}$$

The remaining terms are higher order. Notice that

$$\begin{aligned} f'''(\phi_{max}) =& \int_0^1 \tilde{u}_{\phi_0\phi_0\phi_0}(s;\phi_0)ds\Big|_{\phi_0=\phi_{max}}, \\ g'''(\phi_{max}) =& \int_0^1 \tilde{u}_{\phi_0\phi_0\phi_0}(s;\phi_0)\tilde{\phi}(s;\phi_0)ds + 3\int_0^1 \tilde{u}_{\phi_0\phi_0}(s;\phi_0)\tilde{\phi}_{\phi_0}(s;\phi_0)ds\Big|_{\phi_0=\phi_{max}} \\ =& \phi_{max}f'''(\phi_{max}) + 3\int_0^1 \tilde{u}_{\phi_0\phi_0}(s;\phi_0)\tilde{\phi}_{\phi_0}(s;\phi_0)ds\Big|_{\phi_0=\phi_{max}}, \end{aligned}$$

where we again discard the terms that are zero when $\phi_0 = \phi_{max}$, and also from (4.16)

and Lemma 4.2, one has

$$\begin{aligned}\tilde{u}_{\phi_0\phi_0}(s;\phi_{max}) &= \frac{2}{\mu_l\phi_{max}^2}\int_0^s \tilde{\sigma}(\tau;\phi_{max})\tilde{\phi}_{\phi_0}(\tau;\phi_{max})^2 d\tau \\ &= \frac{(1+\rho_s\phi_{max})(1+B)}{\mu_l\phi_{max}^2}\left[1-(1-s)^{2B+2}\right]. \end{aligned} \tag{4.20}$$

Then

$$a = \frac{1}{2}\int_0^1 \tilde{u}_{\phi_0\phi_0}\left(1-\tilde{\phi}_{\phi_0}\right)ds\Big|_{\phi_0=\phi_{max}} = \frac{(1+\rho_s\phi_{max})B(1+B)}{3\mu_l\phi_{max}^2(2B+3)},$$

$$b = \frac{1}{2}\frac{h_L}{h}\left(\phi_{max}-\phi_L\right)f''(\phi_{max}) = \frac{h_L}{h}\left(\phi_{max}-\phi_L\right)\frac{(1+\rho_s\phi_{max})(1+B)^2}{\mu_l\phi_{max}^2\left(2B+3\right)}.$$

The formula for the roots of the cubic equation (4.19) gives rise to

$$\phi_1^{(1)} = -\frac{b}{3a}\left(1+2\cos\frac{\theta}{3}\right), \quad \phi_1^{(2)} = -\frac{b}{3a}\left(1-\cos\frac{\theta}{3}+\sqrt{3}\sin\frac{\theta}{3}\right),$$

where

$$\theta = \arccos\left(\frac{2b^3+27a^2d}{2b^3}\right).$$

Here we discard the third root as it is positive. Then the specific root chosen for C_L in (4.4) guarantees the entropy conditions (3.5). The expression (4.5) for C_R is carried out in exactly the same manner except that special care is needed in choosing the root to satisfy (3.8). □

On the right of figure 4.1, the slope of dashed lines are calculated using (4.4) and (4.5) for the left and right states respectively, where we can see excellent agreement with the Hogoniot locus when $\frac{1}{h}$ approaches 0.

Figure 4.2 illustrates equation (4.8) and the explanations that follow. The left state is fixed to be $(h_L,\phi_L)=(1,0.5)$, $\phi_R=\phi_L$, and we consider five different values of $h_R: 0.2, 0.15, 0.11, h_R^*=0.09366, 0.05$. The Hugoniot loci are plotted in the $h-\phi_0$ plane on the upper left of figure 4.2 with emphasis on the region $\phi_0>\phi_L$. The next four figures in figure 4.2 are again plotted in $\frac{1}{h}$, where one could easily see that when $h_R>h_R^*$, there is always an intersection near $\frac{1}{h}=0$. This intersection approaches the origin as h_R approaches h_R^* until when $h_R=h_R^*$, the two curves are tangent at $\frac{1}{h}=0$. And when $h_R<h_R^*$, there is no intersection other than the origin. The last figure displays the next order in the asymptotic expression of the Hugoniot loci when $h_R=h_R^*$, i.e., $\phi_{max}-\phi_0-\frac{C_{L/R}h_{L/R}}{h}$ versus $\frac{1}{h^2}$, where one could see that the locus connecting for the left state stays above zero, meaning that the curve $\phi_{max}-\phi_0$ is concave up with respect to $\frac{1}{h}$; while the locus connecting to the right state is concave down with respect to $\frac{1}{h}$. Therefore, they are only tangent at $\frac{1}{h}=0$. This confirms the absence of a double shock solution for this value of h_R.

4.2. Local structure of the singular shock. In this section, we explore the local structure and properties of the singular shock. First we recall a theorem regarding the growth rate of the singular mass and rewrite it in the notation specific to our system.

THEOREM 4.4. *For any $\delta>0$, define the singular mass*

$$M_h(t) = \int_{|x-st|<\delta} h(t,x)dx, \quad M_n(t) = \int_{|x-st|<\delta} n(t,x)dx, \tag{4.21}$$

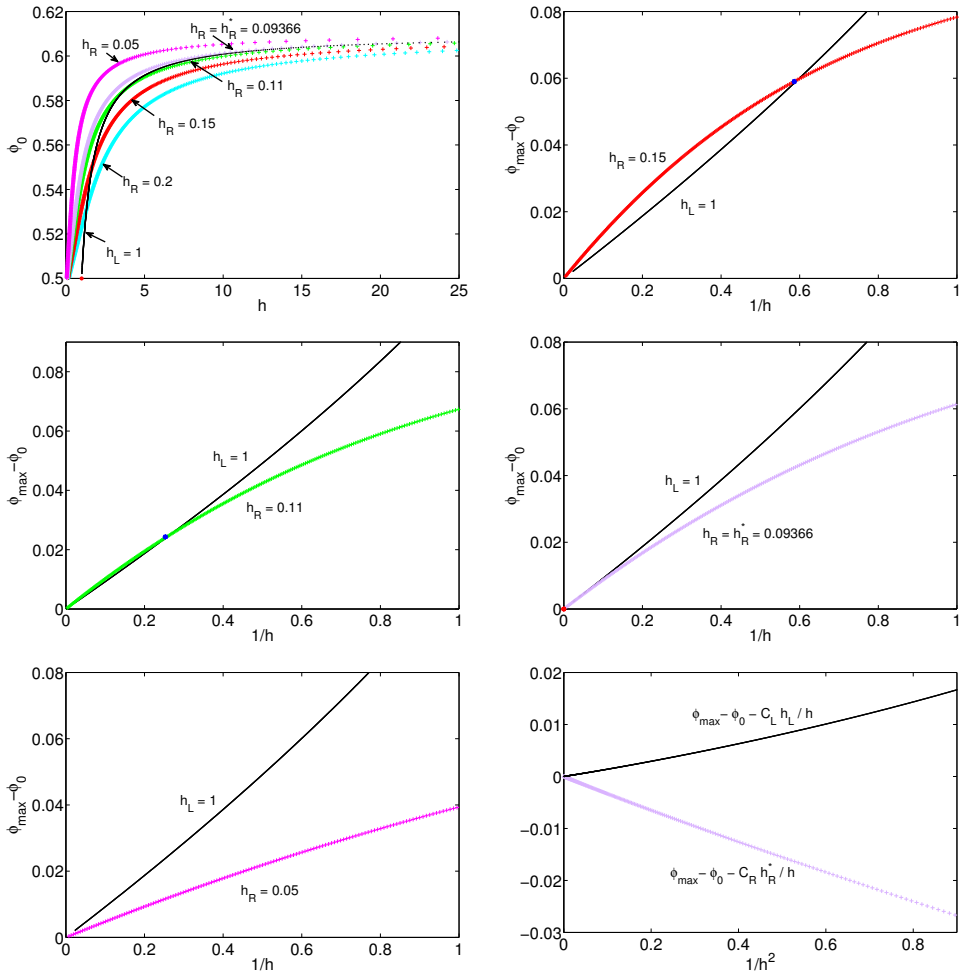

FIG. 4.2. *The Hugoniot loci for left state* $(h_L, \phi_L) = (1, 0.5)$ *and right state with* $\phi_R = \phi_L$ *but different* $h_R = 0.2, 0.15, 0.11, h_R^*(0.09366), 0.05$. *Upper left: regular plot in the* $h - \phi_0$ *plane. The next four figures from left to right and top to bottom: plot of* $\phi_{max} - \phi_0$ *versus* $\frac{1}{h}$. *Lower right: plot of* $\phi_{max} - \phi_0 - \frac{C_{L/R} h_{L/R}}{h}$ *versus* $\frac{1}{h^2}$ *when* $h_R = h_R^*$. *Here angle* $= 30°$.

with s *denoting the shock speed. Then the growth rate satisfies*

$$\frac{dM_h}{dt} = s[h] - \left[h^3 f\left(\frac{n}{h}\right)\right], \quad \frac{dM_n}{dt} = s[n] - \left[h^3 g\left(\frac{n}{h}\right)\right]. \tag{4.22}$$

where $[\star] = \star_R - \star_L$. This theorem has been proved in different frameworks with various regularizations [29]. In fact, this can be formally understood in a very simple way [25]. Choose a parallelogram Ω along $x = st$ as depicted in figure 4.3, then conservation of the total mass in Ω gives rise to

$$\begin{aligned} 0 &= \int (h, h^3 f) \cdot \hat{n}_1 d\Gamma_1 + \int (h, h^3 f) \cdot \hat{n}_2 d\Gamma_2 + \int (h, h^3 f) \cdot \hat{n}_3 d\Gamma_3 + \int (h, h^3 f) \cdot \hat{n}_4 d\Gamma_4 \\ &= -\int_{|x - st_1| < \delta} h dx \; + \; \delta_1 \left[-sh_R + \left(h^3 f\right)_R\right] + \int_{|x - st_2| < \delta} h dx \; - \; \delta_1 \left[-sh_L + \left(h^3 f\right)_L\right] \end{aligned}$$

which is equivalent to $M_h(t_1+\delta_1)-M_h(t_1)=\delta_1\left(s[h]-\left[h^3 f\right]\right)$. Similarly, one has $M_n(t_1+\delta_1)-M_n(t_1)=\delta_1\left(s[n]-\left[h^3 g\right]\right)$ by mass conservation of the particles. Sending δ_1 to zero immediately implies (4.22), which is usually referred to as a generalized Rankine-Hugoniot condition. However, this relation is not enough to give the full description of the singular shock as it is not closed. For the Keyfitz-Kranzer system, they close this relation by noting that the singular mass for the first component vanishes. However, this in general is not true and obviously not applicable to our system. Inspired by the trends in figure 4.2, we notice that ϕ_0 reaches ϕ_{max} at the

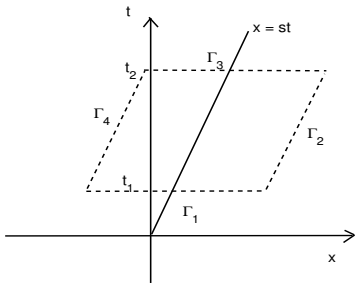

FIG. 4.3. *A parallelogram parallel to $x=st$ with width 2δ and height δ_1.*

place where the singularity occurs. Then from the definitions (4.21), we have the constitutive relation

$$M_n(t)=\phi_{max}M_h(t), \tag{4.23}$$

which gives us a closed relation for the singularity. This constitutive relation makes sense physically as experimental observations show that the particles concentrate tightly at the ridge. However, a rigorous derivation is still lacking and we believe it is relevant to study the vanishing viscosity limit with surface tension and the normal component of gravity. As a result, we have the following formula regarding the singular shock speed when $\phi_R=\phi_L>\phi_{crit}$:

$$s=\frac{\left(h_L^2+h_R^2+h_L h_R\right)\left(\phi_{max}f(\phi_L)-g(\phi_L)\right)}{\phi_{max}-\phi_L}. \tag{4.24}$$

To illustrate this, let

$$h(0,x)=\begin{cases}1 & x<0\\ 10^{-10} & x>0\end{cases},\quad \phi_0(0,x)=0.5,\quad n(0,x)=\phi_0(0,x)h(0,x). \tag{4.25}$$

Figure 4.4 gives the profile of h and n at time $t=600$ as well as the growth of the singular mass M_h and M_n with time. Here we use a moving mesh with speed $s=0.0222$ obtained from (4.24), where one sees that the profile remains stationary in this frame. And (4.22) indicates $\frac{dM_h}{dt}=1.008e-3$ and $\frac{dM_n}{dt}=6.1579e-4$, which matches the the slope of M_h and M_n perfectly.

Moreover, the singular shock speed is checked to satisfy the over-compressive condition [27]:

$$\lambda_L^{(2)}>\lambda_L^{(1)}>s>\lambda_R^{(2)}>\lambda_R^{(1)}, \tag{4.26}$$

where $\lambda_{L/R}^{(1/2)}$ are the eigenvalues of (2.9).

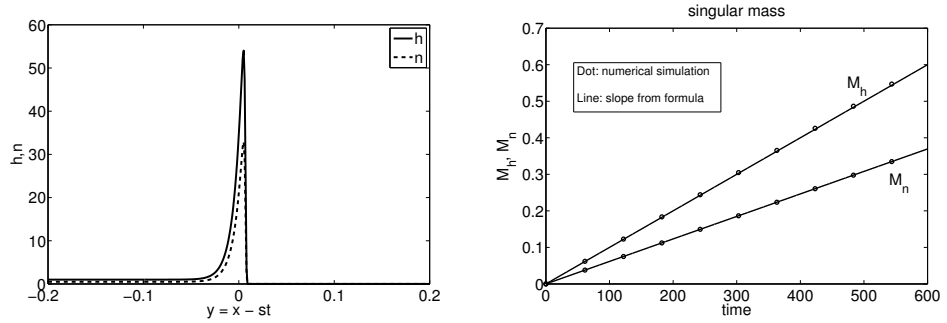

FIG. 4.4. *Simulation of (2.8) using upwind scheme with initial data (4.25) using a moving mesh $y = x - st$ with $s = 0.0222$ calculated from (4.24). Left: the profiles of h and n at time $t = 600$ (corresponding to 0.2 min). Right: the plots of singular mass versus time. The dots are numerical results and the solid line ares calculated by (4.22). Here $\Delta y = 1e-3$, Δt is chosen adaptively to satisfy the CFL condition.*

4.3. Transition from double shock to singular shock. As already mentioned in the last section, the transition from double shock to singular shock happens at the threshold value h_R^*, and moreover, we have

$$\lim_{h_R \to h_R^*} h_M = \infty, \tag{4.27}$$

which can be seen from the trend in figure 4.2. In fact, we can expand the Hugoniot locus to the next order to see its convexity near $\frac{1}{h} = 0$ so as to confirm that the Hugoniot loci will intersect for $h > h_R^*$ and when $h = h_R^*$, they are only tangent at $h = \infty$. For example, for the Hugoniot locus connecting to the left state, write $\phi_2 = \phi_1 + C_L \frac{h_L}{h}$. Then plug $\phi_1 = \phi_2 - C_L \frac{h_L}{h}$ into equation (4.18) and collect the terms of $O\left(\frac{1}{h^4}\right)$ to get the following expression for ϕ_2

$$\begin{aligned}\phi_2 &= \frac{\frac{1}{24}C_L^4\left(\phi_{max}f^{(4)} + 4f'' - g^{(4)}\right) - \frac{1}{6}C_L^3\left(g''' - \phi_L f'''\right) + C_L f_L + f_L\phi_L - g_L}{C_L\left(g'' - \phi_L f''\right) - \frac{1}{2}\left(f''' + 3f'' - g'''\right)}\left(\frac{h_L}{h}\right)^2 \\ &= K_L\left(\frac{h_L}{h}\right)^2,\end{aligned} \tag{4.28}$$

where all the derivatives of f and g are evaluated at ϕ_{max}. We note that $-K_L h_L^2$ matches the slope in the last picture of figure 4.2 for $\phi_L = 0.5$ and remains positive for all $\phi_L > \phi_{crit}$. The corresponding ones for the right states remain negative, thus having opposite convexity from the left ones. As a consequence, we have the following proposition about the transition of the shock speed.

PROPOSITION 4.5. *Given a left and right state (h_L, ϕ_L) and (h_R, ϕ_R) with $\phi_L = \phi_R > \phi_{crit}$ and $h_R < h_L$. Denote by $s_1(h_L, h_R, \phi_L)$ and $s_2(h_L, h_R, \phi_L)$ the 1- and 2-shock speed for the double shock solutions, then*

$$\lim_{h_R \to h_R^*} s_1 = \lim_{h_R \to h_R^*} s_2, \tag{4.29}$$

where h_R^* is the critical value obtained from (4.8).

Proof. Denote (h_M, ϕ_M) the intermediate state, then from the Rankine-Hugoniot condition, one has

$$s_1 = \frac{h_M^3 f(\phi_M) - h_L^3 f(\phi_L)}{h_M - h_L}. \tag{4.30}$$

Then in the limit of $h_R \to h_R^*$, h_M approaches ∞, and thus

$$\lim_{h_R \to h_R^*} s_1 = \lim_{h_R \to h_R^*} h_M^2 f(\phi_M) = \lim_{h_M \to \infty} h_M^2 f\left(\phi_{max} - \frac{h_L}{h_M} C_L(\phi_L)\right) = \frac{1}{2} f''(\phi_{max}) h_L^2 C_L^2, \quad (4.31)$$

where the last equality is obtained using Lemma 4.3. Similarly, we have

$$\lim_{h_R \to h_R^*} s_2 = \frac{1}{2} f''(\phi_{max}) {h_R^*}^2 C_R(\phi_L)^2, \quad (4.32)$$

and since $C_R(\phi_L) h_R^* = C_L(\phi_L) h_L$ from (4.8), the conclusion immediately follows. □

Next, we show that when the double shock speeds coincide, they equal the singular shock speed in figure 4.5. That is, $s_1(h_R^*) = s_2(h_R^*) = s(h_R^*)$ with $s(h_R^*)$ calculated from (4.24). Fix $h_L = 1$, change $\phi_L \in (\phi_{crit}, \phi_{max})$ but keep $\phi_R = \phi_L$. We first calculate the threshold h_R^* according to (4.8), and then plot both $s_1 (= s_2)$ and s with respect to ϕ_L, where one sees a perfect match. This, to some extent, indicates the well-posedness of the hyperbolic system even in the presence of singular shocks.

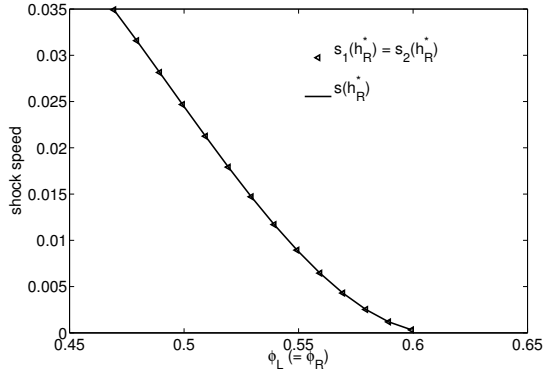

FIG. 4.5. *Comparison of the double shock speeds with the singular shock speed for the left state* $(h_L = 1, \phi_L)$ *with* ϕ_L *changing in* $(\phi_{crit}, \phi_{max})$ *and the right state* $(h_R^*, \phi_R = \phi_L)$. *The double shock speeds* s_1 *(which automatically equals* s_2*) is calculated using (4.31), and the singular shock speed* s *is obtained using (4.24).*

To better observe the transition for the shock speed and mass accumulation rate, we present numerical results in figure 4.6. For a fixed left state, we vary the precursor thickness h_R. The upper left figure represents the shock speed, where one can clearly observe the transition: as h_R approaching h_R^*, the two speeds s_1 and s_2 approach each other until they coincide at the formation of the singular shock. The upper right figure displays the mass accumulation rate in the particle-rich ridge. For the double shock solution, this rate is

$$\frac{dM_h}{dt} = (s_2 - s_1) h_M, \quad \frac{dM_n}{dt} = (s_2 - s_1) n_M, \quad (4.33)$$

and for the singular shock solution, the rate is given in (4.22). Here an interesting observation is that the mass accumulation rate undergoes a continuous transition. The lower two figures in figure 4.6 display the trend as $h \to h_R^*$, where $h_M \to \infty$ and $\phi_M \to \phi_{max}$ are observed as expected.

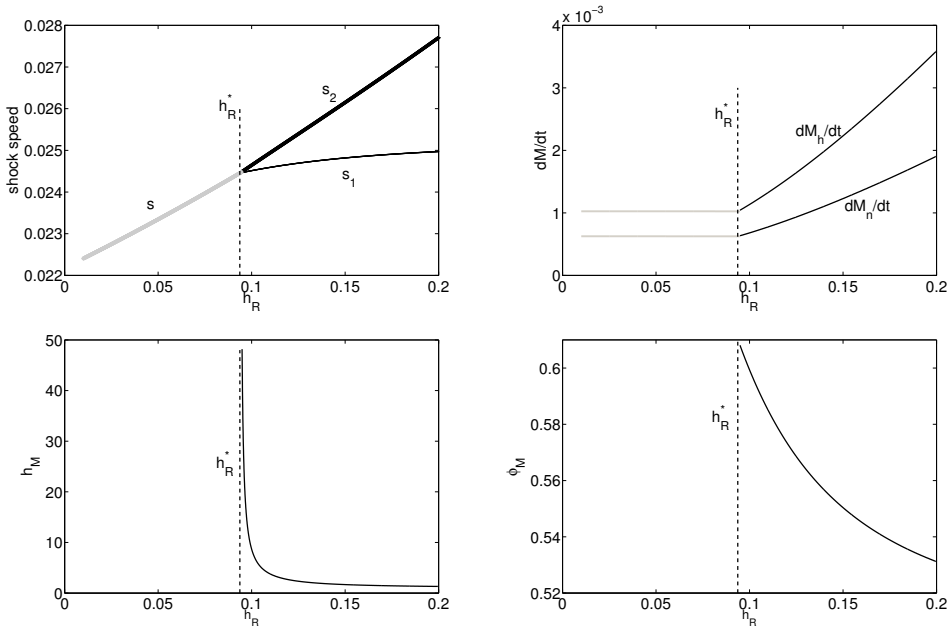

FIG. 4.6. *Upper left: Plots of the shock speeds versus the thickness of the precursor h_R. s_1 and s_2 denote the 1- and 2- shock speeds of the double shock solution calculated by the classical Rakine-Hugoniot condition. s denotes the singular shock speed using (4.24). Upper right: rate of change of mass as described in (4.33) for the double shock solution and (4.22) for the singular shock. Lower left: intermediate h_M w.r.t h_R. Lower right: intermediate ϕ_M w.r.t. h_R. Here angle $= 30°$, left state $(h_L, \phi_L) = (1, 0.5)$ and $\phi_R = \phi_L$. x-axis: the precursor thickness h_R.*

5. Extension to the case $\phi_R < \phi_L$. When $\phi_L > \phi_R > \phi_{crit}$, the previous results can be directly extended since the topology of the Hugoniot locus stays the same when $\phi_0 > \phi_{crit}$. The other situation when $\phi_L > \phi_{crit} > \phi_R$ has different behavior and we will focus on it in this section. At the beginning, let us point out that Theorem 4.4 and equation (4.24) can be directly applied to give the following a priori result as long as the solution is a singular shock.

THEOREM 5.1. *Given a left state (h_L, ϕ_L) and a right state (h_R, ϕ_R) with $\phi_L > \phi_{crit}$ and $h_R < h_L$, if the solution is a singular shock, then the shock speed is*

$$s = \frac{[h^3 g(\phi_0)] - \phi_{max}[h^3 f(\phi_0)]}{[n] - [h]\phi_{max}}, \tag{5.1}$$

where $[\star]$ again denotes $[\star] = \star_R - \star_L$. The proof is omitted as it directly comes out of Theorem 4.4 with the constitutive relation (4.23). It is important to mention that this theorem does not give any information about when there is a singular shock or not. We again resort to the Hugoniot locus to see the formation of a singular shock. This time we fix the precursor thickness but change the particle fraction ϕ_R. Figure 5.1 displays the Hugoniot loci for the left state $(h_L, \phi_L) = (1, 0.5)$ and the right states with $h_R = 0.02$ and $\phi_R = \{0.4, 0.262, 0.2, 0.1\}$. Here black and grey curves represent admissible 1- and 2- shock for the left state. Dashed dots represent the admissible 2-wave for the right states. Special attention should be paid to the dashed curve which denotes the *over-compressive* shock connecting to the left state. That is, the

states (h, ϕ_0) satisfying

$$\lambda^{(2)}(h_L, \phi_L) > \lambda^{(1)}(h_L, \phi_L) > s > \lambda^{(2)}(h, \phi_0) > \lambda^{(1)}(h, \phi_0). \tag{5.2}$$

Although the Hugoniot locus connecting to any right state intersect the black curve, not all intersection points give the physical intermediate states. Indeed, when $\phi_R > \phi_R^*$, the intersection point (the open symbols in figure 5.1) yields a 1-shock speed larger than the 2-shock speed, which violates the physics. When $\phi_R < \phi_R^*$, there is an entropy satisfying double shock solution with intermediate state (h_M, ϕ_M) (the solid dots in figure 5.1) such that $h_M < \min\{h_L, h_R\}$ and $\phi_M < \min\{\phi_L, \phi_R\}$, as in the settled case. And ϕ_R^* lies on the over-compressive part of the Hugoniot locus for the left state! This could be more clearly observed in figure 5.2 on the left, where 1- and 2-shock speeds are calculated directly from the classical jump condition. One sees that when $\phi_R > \phi_R^*$, we can still satisfy the classical Rankine-Hugoniot jump condition but with $s_1 > s_2$, thus this should be discarded and replaced by the singular shock with speed calculated by (5.1). Figure 5.2 on the right demonstrates the changing rate of the mass accumulation, where an important difference from figure 4.6 is that at the transition point the mass accumulation rate is zero, that is, the left and right state are directly connected by one over-compressive shock without an intermediate state. This is like the classical formulation of the singular shock in the Keyfitz-Kranzer system [16, 15]. Therefore, the observation for $\phi_L > \phi_{crit} > \phi_R$ can be summarized as follows.

In summary, for a given (h_L, ϕ_L) and (h_R, ϕ_R) with $\phi_L > \phi_{crit}$, $h_L > h_R$, $\phi_L > \phi_R$, if (h_R, ϕ_R) lies on the left of the dashed curve in figure 5.2, there is a singular shock.

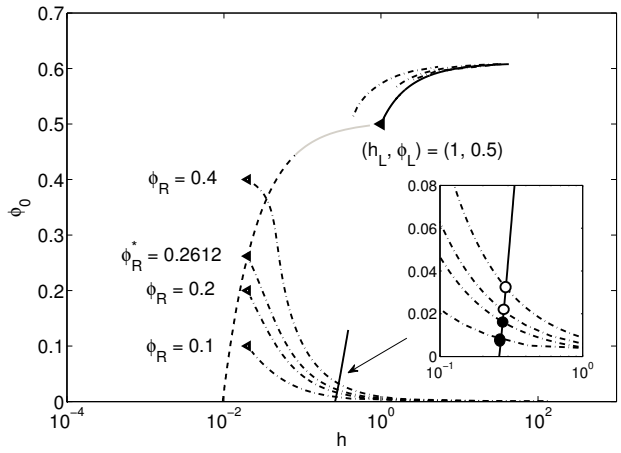

FIG. 5.1. *The Hugoniot loci for left state $(h_L, \phi_L) = (1, 0.5)$ and right states with $h_R = 0.02$ and $\phi_R = \{0.4, 0.262, 0.2, 0.1\}$. The black and grey curves represent admissible 1- and 2- shocks for the left state, and the dashed curve represents an* over-compressive *shock connecting to the left state. Dashed dots denote an admissible 2-shock connecting to the right states. Here the angle $\alpha = 30°$.*

We close this section by showing the solution of the Riemann problem (2.8) with $h_L = 1$, $\phi_L = 0.5$, $h_R = 0.02$ and $\phi_R = \{0.25, \phi_R^* = 0.2612, 0.27\}$ in figure 5.3, where one could easily see the transition from double shock solution to singular shock solution.

6. Conclusion. We study the shock solutions for the Riemann problem of a lubrication model describing the particle-laden thin films down an incline. When the particle

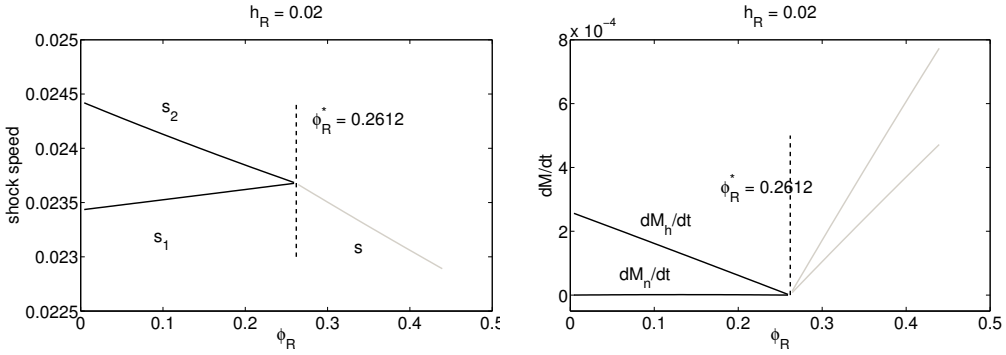

FIG. 5.2. *Left: 1- and 2- shock speeds calculated directly from the Rankine-Hugoniot condition. Right: changing rate of the mass accumulation. Here the angle* $\alpha = 30°$*, the left state* $(h_L, \phi_L) = (1, 0.5)$*, the right state* $h_R = 0.02$ *and* $\phi_R \in [0, \phi_{crit})$*.*

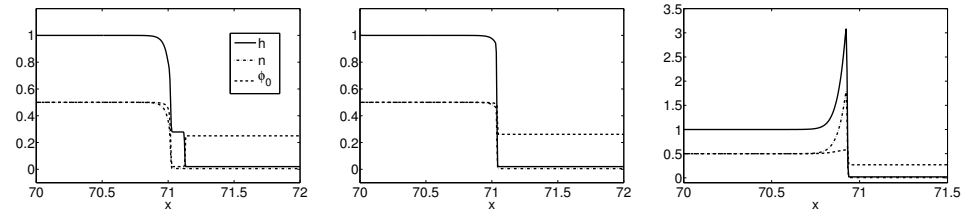

FIG. 5.3. *Profiles of* h*,* n *and* ϕ *obtained by solving (2.8) numerically. Here the angle* $\alpha = 30°$*. Fix* $(h_L, \phi_L) = (1, 0.5)$*, and* $h_R = 0.02$*. tFinal* $= 1min$*. Left:* $\phi_R = 0.25$*. Middle:* $\phi_R = \phi_R^* = 0.2612$*. Right:* $\phi_R = 0.27$*.*

concentration is above a critical value, the particles will move to the contact line of the flow and form a particle-rich ridge. This could be explained mathematically by a double shock or singular shock depending on the concentration and thickness of the precursor. If the precursor has the same concentration as the bulk flow, the thickness of the precursor determines whether the solution is a double shock or a singular shock. The formation of the singular shock is analyzed through a detailed study of the asymptotic behavior of the Hugoniot locus for large values of h. A threshold for the thickness of the precursor is also derived as a byproduct, and the transition from a double shock to a singular shock happens when two shock speeds coincide and the intermediate height approaches infinity. We also obtain a formula for the singular shock speed by noticing that particles concentrate at the maximum packing fraction in this case. When the precursor has a different concentration from the bulk flow, two possible behaviors are observed. In one case when the concentration in the precursor is still above the critical value, all the previous results can be directly applied. In the other case when the concentration is below the critical value, we observe a different transition while the formula for the shock speed is derived in the same argument as before. This work is the first detailed study of singular shock formation in this model and the first rigorous study of the system of conservation laws (2.6). The results are a combination of rigorous, asymptotic, and careful numerical results and also suggest a number of open problems.

Acknowledgements. The first author would like to thank Dr. Aliki Mavromoustaki for helpful discussions especially the nice explanations of the model and background.

REFERENCES

[1] A. Acrivos, G. K. Batchelor, E. J. Hinch, D. L. Koch, and R. Mauri. Longitudinal shear-induced diffusion of spheres in a dilute suspension. *J. Fluid. Mech.*, 240:651, 1992.

[2] A. L. Bertozzi, J. L. Rosado, M. B. Short, and L. Wang. Contagion shocks in one dimension. in preparation.

[3] F. Bouchut. *On zero pressure gas dynamics.* in Advances in Kinetic Theory and Computing, Ser. Adv. Math. Appl. Sci. World Science Publishing, River Edge, NJ, 1994.

[4] J.F. Brady. The rheological behavior of concentrated colloidal dispersions. *J. Chem. Phys.*, 99:567, 1993.

[5] Y. Brenier and E. Grenier. Sticky particles and scalar conservation laws. *SIAM J. Numer. Anal.*, 35:2317–2328, 1998.

[6] G. Chen and H. Liu. Formation of δ-shocks and vacuum states in the vanishing pressure limit of solutions to the Euler equations for isentropic fluids. *SIAM J. Math. Anal.*, 34(4):925–938, 2003.

[7] B. Cook. Theory for particle settling and shear-induced migration in thin-film liquid flow. *Phys. Rev. E*, 78:045303, 2008.

[8] B. Cook, A. Bertozzi, and A. Hosoi. Shock solutions for particle-laden thin films. *SIAM J. Appl. Math*, 68:760–783, 2008.

[9] C. M. Dafermos. Solution of the Riemann problem for a class of hyperbolic systems of conservation laws by the viscosity method. *Arch. Rat. Mech. Anal.*, 52:1–9, 1973.

[10] C. M. Dafermos and R. J. DiPerna. The riemann problem for certain classes of hyperbolic systems of conservation laws. *J. Differential Equations*, 20:90–114, 1976.

[11] V. G. Danilov and V. M. Shelkovich. Delta-shock wave type solution of hyperbolic systems of conservation laws. *Quart. Appl. Math.*, 63:401–427, 2005.

[12] R. H. Davis and A. Acrivos. Sedimentation of non colloidal particles at low reynolds numbers. *Annu. Rev. Fluid Mech.*, 17:91–118, 1985.

[13] H. E. Huppert. Flow and instability of a viscous current down a slope. *Nature*, 300:427–429, 1982.

[14] B. L. Keyfitz and H. C. Kranzer. A viscosity approximation to a system of conservation laws with no classical riemann solution. *Proceedings of International Conference on Hyperbolic Problems, Bordeaux*, 1988.

[15] B. L. Keyfitz and H. C. Kranzer. Spaces of weighted measures for conservation laws with singular shock solutions. *Jour. Diff. Eqns.*, 118(2):420–451, 1995.

[16] H. C. Kranzer and B. L Keyfitz. A strictly hyperbolic system of conservation laws admitting singular shocks, in nonlinear evolution equations that change type. *IMA Vol. Math. Appl.*, 27:107–125, 1990.

[17] P. D. Lax. *Hyperbolic system of conservation laws and the mathematical theory of shock waves.* CBMS-NSF Regional Conference Series in Applied Mathematics. SIAM, 1987.

[18] S. Lee, Y. Stokes, and A. L. Bertozzi. A model for particle laden flow in a spiral concentrator, 2012 in beijing. *Proceedings of International Conference on Theoretical and Applied Mechanics*, 2012. Beijing.

[19] D. Leighton and A. Acrivos. The shear-induced migration of particles in concentrated suspensions. *J. Fluid. Mech.*, 181:415, 1987b.

[20] A. Mavromoustaki and A. L. Bertozzi. Hyperbolic systems of conservation laws in gravity-driven, particle-laden thin-film flows. *J. Engineering Math.* submitted.

[21] C. Mouquet, V. Greffeuille, and S. Treche. Characterization of the consistency of gruels consumed by infants in developing countries: Assessment of the bostwick consistometer and comparison with viscosity measurements and sensory perception. *Int. J. Food Sci. Nutr.*, 57:459, 2006.

[22] N. Murisic, J. Ho, V. Hu, P. Latterman, T. Koch, K. Lin, M. Mata, and A.L. Bertozzi. Particle-laden viscous thin-films on an incline: Experiments compared with a theory based on shear-induced migration and particle settling. *Physica D: Nonlinear Phenomena*, 204(20):1661–1673, 2010.

[23] N. Murisic, B. Pausader, D. Peschka, and A.L. Bertozzi. Dynamics of particle settling and resuspension in viscous liquids. *J. Fluid Mech.*, 717:203–231, 2013.

[24] M. Nedeljkov. Delta and singular delta locus for one-dimensional systems of conservation laws. *Math. Methods Appl. Sci.*, 27(8):931–955, 2004.

[25] R. Sanders and M. Sever. The numerical study of singular shocks regularized by small viscosity. *Journal of Sci. Comput.*, 19(1–3):385–404, 2003.

[26] D. G. Schaeffer, S. Schecter, and M. Shearer. Nonstrictly hyperbolic conservation laws with a parabolic line. *Journal of Differential Equations*, 103:94–126, 1993.

[27] D. G. Schaeffer and M. Shearer. Riemann problems for nonstrictly hyperbolic 2×2 system of conservation laws. *Trans. A. M. S.*, 301:267–306, 1987.

[28] M. Sever. Viscous structure of singular shocks. *Nonlinearity*, 15:705–725, 2002.

[29] M. Sever. *Distribution solutions of nonlinear systems of conservation laws*. Mem. Amer. Math. Soc., 2007.

[30] D. Tan, T. Zhang, and Y. Zheng. Delta-shock waves as limits of vanishing viscosity for hyperbolic systems of conservation laws. *J. Differential Equations*, 112:1–32, 1994.

[31] Thomas Ward, Chi Wey, Robert Glidden, A. E. Hosoi, and A. L. Bertozzi. Experimental study of gravitation effects in the flow of a particle-laden thin film on an inclined plane. *Physics of Fluids*, 21:083305, 2009.

[32] J.C. Van Der Werff and C. G. De Kruif. Hard-sphere colloidal dispersions: The scaling of rheological properties with particle size, volume fraction, and shear rate. *J. Rheol*, 33(3):421–455, 1989.

[33] H. Yang. Riemann problems for a class of coupled hyperbolic systems of conservation laws. *J. Differential Equations*, 159(2):447–484, 1999.

[34] J. Zhou, B. Dupuy, A. L. Bertozzi, and A. E. Hosoi. Theory for shock dynamics in particle-laden thin films. *Physical Review Letters*, 94:117803, 2005.